Towards a QMC-based density functional including finite-range effects: excitation modes of a ^{39}K quantum droplet

V. Cikojević,[1,2] L. Vranješ Markić,[1] M. Pi,[3,4] M. Barranco,[3,4] and J. Boronat[2]

[1] *University of Split, Faculty of Science, Ruđera Boškovića 33, HR-21000 Split, Croatia*
[2] *Departament de Física, Universitat Politècnica de Catalunya, Campus Nord B4-B5, E-08034 Barcelona, Spain*
[3] *Departament FQA, Facultat de Física, Universitat de Barcelona, Diagonal 645, 08028 Barcelona, Spain*
[4] *Institute of Nanoscience and Nanotechnology (IN2UB), Universitat de Barcelona, 08028 Barcelona, Spain*

(Dated: September 1, 2020)

Some discrepancies between experimental results on quantum droplets made of a mixture of ^{39}K atoms in different hyperfine states and their analysis within extended Gross-Pitaevskii theory (which incorporates beyond mean-field corrections) have been recently solved by introducing finite-range effects into the theory. Here, we study the influence of these effects on the monopole and quadrupole excitation spectrum of extremely dilute quantum droplets using a density functional built from first-principles quantum Monte Carlo calculations, which can be easily introduced in the existing Gross-Pitaevskii numerical solvers. Our results show differences of up to 20% with those obtained within the extended Gross-Pitaevskii theory, likely providing another way to observe finite-range effects in mixed quantum droplets by measuring their lowest excitation frequencies.

I. INTRODUCTION

Ultracold gases serve as a unique platform for understanding quantum many-body physics [1]. This notoriously hard problem is often reduced to the effective single-particle picture when the interactions are very weak and the density is very low [2, 3]. Because of its simplicity and predictive power, the mean field approach has become a standard (or a first starting point) to study the properties of ultracold gases.

The accuracy of mean-field theories to address dilute quantum gases is expectable, as nearly all experiments are performed at very low values of the gas parameter ρa^3, ρ being the atom number density and a the s-wave scattering length describing the interparticle interactions. This allows for a perturbative approach à la Bogoliubov [4], where static and dynamic properties are well described by the Gross-Pitaevskii equation. However, as the density and/or the interaction strength increases, the system becomes more correlated and out of the range of applicability of perturbation theories. It is a priori difficult to know when the perturbative approach is no longer valid. Thus, it is essential to supplement the theory with developments [5–15] aiming at verifying the range of applicability of the mean-field approach and disclosing the role played by higher-order effects.

A promising system for investigating quantum many-body effects, going beyond mean-field theory, is the self-bound Bose-Bose mixture first proposed by Petrov [16]. In this mixture, with repulsive intraspecies and attractive interspecies short-range interactions, the unstable attractive mean-field energy is balanced out by a repulsive beyond mean-field term (the Lee-Huang-Yang (LHY) term) [17], resulting in a liquid droplet resembling the well-known ^{4}He droplets [18], but with a far smaller density. So far, a Bose-Bose droplet state has been observed in a mixture of two ^{39}K hyperfine states [19–21], and in an heterogeneous mixture of ^{41}K-^{87}Rb atoms [22].

In the first experimental observation [19], discernible differences were observed between the experiment and the results of the mean-field (MF) theory extended with an LHY term. Quite recently, it has been reported [23] that the agreement between theory and experiment improves notably when finite-range effects are properly taken into account. For the particular mixture of two hyperfine states of ^{39}K atoms, we know two scattering parameters in each of the interaction channels [24], the s-wave scattering length a and the effective range $r^{\rm eff}$, which are the first two coefficients in the expansion of the s-wave phase shift in the scattering between two atoms [25]

$$k\cot\delta(k) = -\frac{1}{a} + \frac{1}{2}r^{\rm eff}k^2 + \mathcal{O}(k^4). \qquad (1)$$

The non-zero (in fact quite large) effective ranges open a promising new regime in quantum mixtures which go beyond the usual mean-field theory corrected with the LHY term (MF+LHY) [26–28]. A large effective range means that the interaction between atoms is far from the contact Dirac δ-interaction usually employed for dilute Bose gases.

In a previous work [23], some of us have performed diffusion Monte Carlo (DMC) calculations [29, 30] using model potentials that reproduce both scattering parameters, obtaining the equation of state for a ^{39}K mixture in the homogeneous liquid phase. We concluded that one could reproduce the critical atom number determined in the experiment [19] only for the model potentials which incorporate the correct effective range. This critical number is a static property of the quantum droplet at equilibrium. Besides a good knowledge of the equilibrium properties of a quantum many-body system, determining the excitation spectrum is essential to unveil its microscopic structure.

In the present work, we present a study of the monopole and quadrupole excitation spectrum of a ^{39}K quantum droplet using the QMC functional introduced in Ref. [23], which correctly describes the inner part of large drops, constituting an extension to the MF+LHY theory. The excitation spectrum of these droplets has already been calculated within the MF+LHY approach [16, 31]. Our goal is to make visible the appearance of any beyond-LHY effect arising from the inclusion of the effective range in the interaction potentials.

This paper is organized as follows. We build in Sec. II the QMC density functional, in the local density approximation (LDA), and compare it with the MF+LHY approach, which can be expressed in a similar form. In Sec. III, we give details on the application of the density functional method, static and dynamic, to the obtainment of the ground state and excitation spectrum of quantum droplets. In Sec. IV, we report the results of the monopole and quadrupole frequencies obtained with the QMC functional and compare them with the MF+LHY predictions. Finally, a summary and outlook are presented in Sec. V.

II. THE QMC DENSITY FUNCTIONAL

We shall consider ^{39}K mixtures at the optimal relative atom concentration yielded by the mean-field theory, namely $N_1/N_2 = \sqrt{a_{22}/a_{11}}$ [16]. For these mixtures, we have shown that the energy per atom in the QMC approach can be accurately written as [23]

$$\frac{E}{N} = \alpha\rho + \beta\rho^{\gamma} \ , \tag{2}$$

where ρ is the total atom number density. The parameters α, β, and γ have been determined by fits to the DMC results for the model potentials satisfying the s-wave scattering length and effective range, given in Table I. Parameters appearing in Eq. (2) are collected in Table II, for three values of the magnetic field (B). The QMC approach does not yield a universal expression for E/N, as it depends on the value of the applied B. For the optimal concentration, the MF+LHY energy per particle can be cast in a similar expression

$$\frac{E/N}{|E_0|/N} = -3\left(\frac{\rho}{\rho_0}\right) + 2\left(\frac{\rho}{\rho_0}\right)^{3/2} \ , \tag{3}$$

where E_0/N and ρ_0 are the energy per atom and atom density at equilibrium,

$$E_0/N = \frac{25\pi^2\hbar^2|a_{12}+\sqrt{a_{11}a_{22}}|^3}{768ma_{22}a_{11}\left(\sqrt{a_{11}}+\sqrt{a_{22}}\right)^6} \tag{4}$$

and

$$\rho_0 = \frac{25\pi}{1024a_{11}^3}\frac{\left(a_{12}/a_{11}+\sqrt{a_{22}/a_{11}}\right)^2}{\left(a_{22}/a_{11}\right)^{3/2}\left(1+\sqrt{a_{22}/a_{11}}\right)^4} \ . \tag{5}$$

TABLE I. Scattering parameters, i.e. s-wave scattering length a and effective range $r^{\rm eff}$ (in units of Bohr radius a_0) as a function of B [32].

B(G)	$a_{11}(a_0)$	$r_{11}^{\rm eff}(a_0)$	$a_{22}(a_0)$	$r_{22}^{\rm eff}(a_0)$	$a_{12}(a_0)$	$r_{12}^{\rm eff}(a_0)$
56.230	63.648	-1158.872	34.587	578.412	-53.435	1021.186
56.453	70.119	-1150.858	34.136	599.143	-53.333	1023.351
56.639	76.448	-1142.642	33.767	616.806	-53.247	1025.593

TABLE II. Parameters of the QMC energy per atom calculated at several magnetic fields B, assuming $\rho_1/\rho_2 = \sqrt{a_{22}/a_{11}}$, satisfying the s-wave scattering length a and effective range $r^{\rm eff}$ given in Table I. α is in $\hbar^2a_{11}^2/(2m)$ units, β is in $\hbar^2a_{11}^{3\gamma-2}/(2m)$ units, m being the mass of a ^{39}K atom, and γ is dimensionless.

B(G)	α	β	γ
56.230	-0.812	5.974	1.276
56.453	-0.423	8.550	1.373
56.639	-0.203	12.152	1.440

In Eqs. (4) and (5), m is the mass of a ^{39}K atom and a_{ij} are the three different s-wave scattering lengths. MF+LHY theory is thus universal if it is expressed in terms of ρ_0 and E_0. According to this theory, the droplet properties do not change separately on N and a_{ij} but rather combined through

$$\frac{N}{\tilde{N}} = \frac{3\sqrt{6}}{5\pi^2}\frac{\left(1+\sqrt{a_{22}/a_{11}}\right)^5}{\left|a_{12}/a_{11}+\sqrt{a_{22}/a_{11}}\right|^{5/2}} \ , \tag{6}$$

where $\tilde{N}$ is a dimensionless parameter [16]. Additionally, the healing length corresponding to the mixture is

$$\frac{\xi}{a_{11}} = \frac{8\sqrt{6}}{5\pi}\sqrt{\frac{a_{22}}{a_{11}}}\frac{(1+\sqrt{a_{22}/a_{11}})^3}{\left|a_{12}/a_{11}+\sqrt{a_{22}/a_{11}}\right|^{3/2}} \ . \tag{7}$$

The energy per atom Eq. (2) allows one to readily introduce, within LDA, a density functional whose interacting part is

$$\mathcal{E}_{\rm int} = \rho\frac{E}{N} = \alpha\rho^2 + \beta\rho^{\gamma+1} \ . \tag{8}$$

A similar expression holds in the MF+LHY approach. In the homogeneous phase, one may easily obtain the pressure

$$p(\rho) = \rho^2\frac{\partial}{\partial\rho}\left(\frac{E}{N}\right) = \alpha\rho^2 + \beta\gamma\rho^{\gamma+1} \tag{9}$$

and incompressibility

$$\kappa(\rho) = \rho\frac{\partial p}{\partial\rho}, \tag{10}$$

which can be written as

$$\kappa(\rho) = \rho^2\frac{\partial^2\mathcal{E}_{\rm int}}{\partial\rho^2} = \rho^2\left\{2\frac{\partial}{\partial\rho}\left(\frac{E}{N}\right) + \rho\frac{\partial^2}{\partial\rho^2}\left(\frac{E}{N}\right)\right\}. \tag{11}$$

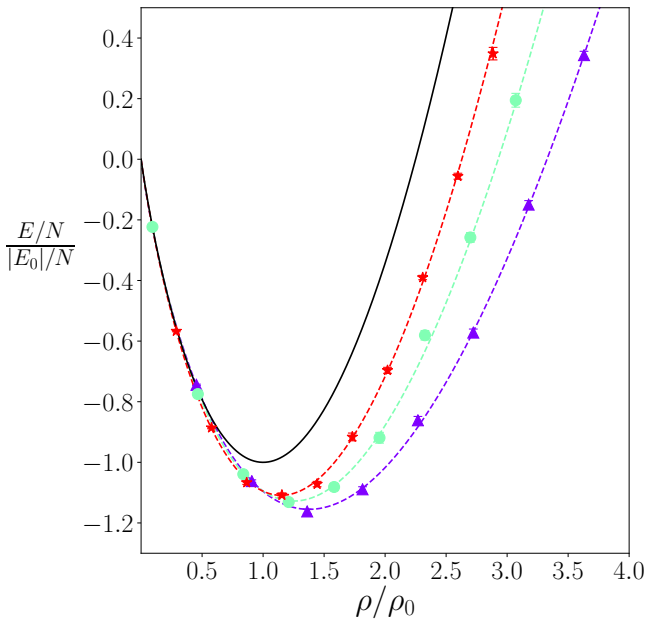

FIG. 1. DMC energy per particle as a function of the density. From bottom (blue triangles) to top (red stars), the results correspond to magnetic fields B=56.23, 56.453 and 56.639 G. Calculations were performed for the mean-field optimal ratio $\rho_2/\rho_1 = \sqrt{a_{11}/a_{22}}$. The energy per atom and atom density are normalized to the $|E_0|/N$ and ρ_0 MF+LHY values obtained from Eqs. (4) and (5), respectively. The dashed lines are fits in the form $E/N = \alpha\rho + \beta\rho^\gamma$. The black solid line corresponds to the MF+LHY theory, Eq. (3).

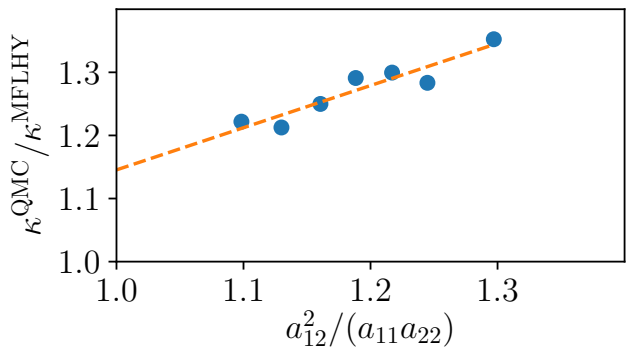

FIG. 2. DMC over MF+LHY incompressibility ratio at equilibrium for the magnetic fields considered in Ref. [23]. The dashed line is a linear fit to the points.

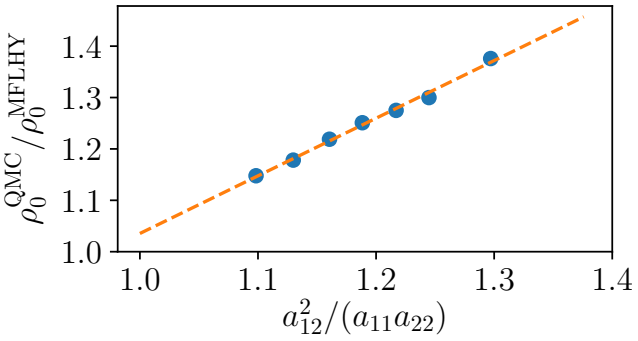

FIG. 3. DMC over MF+LHY equilibrium density ratio for the magnetic fields considered in Ref. [23]. The dashed line is a linear fit to the points.

Figure 1 shows the DMC energy per atom as a function of the density for selected values of the magnetic field, together with the result for the MF+LHY theory. It is worth noticing the rather different equations of state yielded by the QMC functional and MF+LHY approaches. The QMC approach yields a substantially larger equilibrium density and more binding. The QMC incompressibility is also larger, as can be seen in Fig. 2; at first sight, this seems to be in contradiction with the results in Fig. 1, which clearly indicate that the curvature of the E/N vs ρ curve at equilibrium ($\partial(E/N)/\partial\rho = 0$ point) is smaller for the QMC functionals than for the MF+LHY approach. However, this is compensated by the larger QMC value of the atom density at equilibrium, see Eq. (11) and Fig. 3, where we show the ratio of QMC and MF+LHY equilibrium densities. Besides its importance for a quantitative description of the monopole droplet oscillations addressed here, inaccurate incompressibility may affect the description of processes where the liquid-like properties of quantum droplets play a substantial role, as *e.g.* droplet-droplet collisions [33].

Another fundamental property of the liquid is the surface tension σ of the free-surface. Remarkably, for simple functionals as the QMC and MF+LHY ones discussed in this work, its value can be obtained by simple quadrature [34]

$$\sigma = 2\int_0^{\rho_0} d\rho \left[\left(\frac{\hbar^2}{8m}\right)(\alpha\rho + \beta\rho^\gamma - \mu)\right]^{1/2}, \qquad (12)$$

where μ is the chemical potential evaluated at the equilibrium density. The surface tension of several QMC functionals, i.e. functionals corresponding to different magnetic fields, is given in Table III. As can be seen, QMC functionals yield consistently higher values of the surface tension than the MF+LHY approach. Within MF+LHY, the surface tension can be written in terms of the equilibrium density (5) and healing length (7), $\sigma_{\rm MF+LHY} = 3(1+\sqrt{3})\rho_0\hbar^2/(35m\xi)$ [16].

TABLE III. Surface tension of a ^{39}K Bose-Bose mixture at the MF+LHY optimal mixture composition in $10^{-8}\times\hbar^2/(ma_{11}^4)$ units.

B(G)	$\sigma_{\rm MF+LHY}$	$\sigma_{\rm QMC}$
56.230	35.1	48.8
56.453	9.31	12.2
56.639	1.21	1.46

III. THE LDA-DFT APPROACH

A. Statics

Once $\mathcal{E}_{\rm int}[\rho]$ has been obtained, we have used density functional theory (DFT) to address the static and dynamic properties of ^{39}K droplets similarly as for superfluid ^{4}He droplets [35]. Within DFT, the energy of the quantum droplet at the optimal composition mixture is written as a functional of the atom density $\rho(\mathbf{r})$ as

$$E[\rho] = T[\rho] + E_c[\rho] = \frac{\hbar^2}{2m}\int d\mathbf{r}|\nabla\Psi(\mathbf{r})|^2 + \int d\mathbf{r}\,\mathcal{E}_{\rm int}[\rho], \tag{13}$$

where the first term is the kinetic energy, and the effective wavefunction $\Psi(\mathbf{r})$ of the droplet is related to the atom density as $\rho(\mathbf{r}) = |\Psi(\mathbf{r})|^2$. The equilibrium configuration is obtained by solving the Euler-Lagrange equation arising from the functional minimization of Eq. (13)

$$\left\{-\frac{\hbar^2}{2m}\nabla^2 + \frac{\partial\mathcal{E}_{int}}{\partial\rho}\right\}\Psi \equiv \mathcal{H}[\rho]\,\Psi = \mu\Psi, \tag{14}$$

where μ is the chemical potential corresponding to the number of ^{39}K atoms in the droplet, $N = \int d\mathbf{r}|\Psi(\mathbf{r})|^2$.

The time-dependent version of Eq. (14) is obtained minimizing the action and adopts the form

$$i\hbar\frac{\partial}{\partial t}\Psi(\mathbf{r},t) = \mathcal{H}[\rho]\,\Psi(\mathbf{r},t). \tag{15}$$

We have implemented a three-dimensional numerical solver based on the Trotter decomposition of the time-evolution operator with second-order accuracy in the time-step Δt [36]

$$e^{-i\mathcal{H}\Delta t} = e^{-i\Delta t V(\boldsymbol{R}')/2}e^{-i\Delta t K}e^{-i\Delta t V(\boldsymbol{R})/2} + \mathcal{O}(\Delta t^3)\ , \tag{16}$$

with K and V being the kinetic and interaction terms in Eq. (14). Within this scheme, it is possible to obtain both the ground state and the dynamical evolution. Indeed, reformulating the problem via a Wick rotation $t = -i\tau$, the propagation of a wavefunction in imaginary time τ leads to the ground-state equilibrium solution. It is known that in real time, the Trotter decomposition may be unstable for different combinations of time step and space step used in the discretization [37]. We have carefully chosen the time step that makes the dynamic evolution stable during the time we have propagated the static initial configuration.

Figure 4 shows the density profile of two droplets, one corresponding to a small gaussian-like droplet and the other to a large saturated one. They have been obtained within the QMC ($B = 56.230$ G) functional and MF+LHY methods. The sizeable difference between the profiles yielded by both approaches reflects the different value of their equilibrium densities, see Fig. 3.

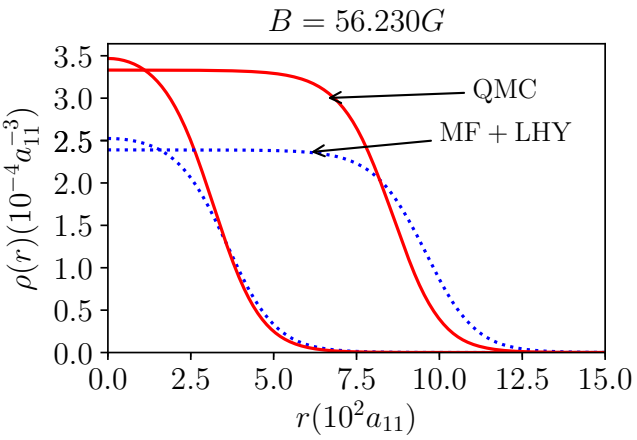

FIG. 4. Density profiles of two ^{39}K quantum droplets corresponding to a small $(\tilde{N}-\tilde{N}_c)^{1/4} = 3$, and to a large droplet $(\tilde{N}-\tilde{N}_c)^{1/4} = 6$, where $\tilde{N}_c = 18.65$ is the critical number below which the droplet becomes unstable within the MF+LHY theory [16]. Solid lines, QMC functional; dotted lines, MF+LHY approach.

B. Real-time dynamics and excitation spectrum

The multipole excitation spectrum of a quantum droplet can be obtained *e.g.* by solving the equations obtained linearizing Eq. (15) [16, 38, 39]. We have used an equivalent method based on the Fourier analysis of the real-time oscillatory response of the droplet to an appropriated external field [40, 41]. The method, which we outline now, bears clear similarities with the experimental procedure to access to some excited states of confined Bose-Einstein condensates (BEC) [42, 43]. For monopole oscillations, our method is similar to that used in Ref. [44].

A droplet at the equilibrium, whose ground-state effective wavefunction $\Psi(\mathbf{r})$ is obtained by solving the DFT Eq. (14), is displaced from it by the action of a static external one-body field Q whose intensity is controlled by a parameter λ. The new equilibrium wavefunction $\Psi'(\mathbf{r})$ is determined by solving Eq. (14) for the constrained Hamiltonian $\mathcal{H}'$

$$\mathcal{H} \to \mathcal{H}' = \mathcal{H} + \lambda Q. \tag{17}$$

If λ is small enough so that λQ is a perturbation and linear response theory applies, switching off Q and letting $\Psi'(\mathbf{r})$ evolve in time according to Eq. (15), $\langle Q(t)\rangle$ will oscillate around the equilibrium value $Q_{eq} = \langle\Psi(\mathbf{r})|Q|\Psi(\mathbf{r})\rangle$. Fourier analyzing $\langle Q(t)\rangle$, one gets the non-normalized strength function corresponding to the excitation operator Q, which displays peaks at the frequency values corresponding to the excitation modes of the droplet. Specific values of λ that we use are in the range from $\lambda = 10^{-13}$ to 10^{-15} for the monopole modes, and $\lambda = 10^{-15}$ to 10^{-17} for the quadropole modes, with λ being measured in $\hbar^2/(2ma_{11}^4)$ units, and the smaller

values corresponding to larger magnetic fields, i.e. less correlated drops.

IV. RESULTS

We have used as excitation fields the monopole Q_0 and quadrupole Q_2 operators

$$Q_0 = \sum_i^N r_i^2 \tag{18}$$

$$Q_2 = \sum_i^N \left(r_i^2 - 3z_i^2\right) \tag{19}$$

which allows one to obtain the $\ell = 0$ and 2 multipole strengths. The $\ell = 0$ case corresponds to pure radial oscillations of the droplet and for this reason it is called "breathing" mode. In a pure hydrodynamical approach, its frequency is determined by the incompressibility of the liquid and the radius of the droplet [3, 45].

We have propagated the excited state $\Psi'(\mathbf{r})$ for a very long period of time, storing $\langle Q(t)\rangle$ and Fourier analyzing it. Fig. 5 (left) shows $\langle Q_0(t)\rangle$ for ^{39}K quantum droplets of different sizes. We choose the same scale of particle numbers (x-axis) as in Ref. [16], as the monopole frequency ω_0 close to the instability point $\tilde{N}_c = 18.65$ is directly proportional to $(\tilde{N}-\tilde{N}_c)^{1/4}$ [16]. Whereas a harmonic behavior is clearly visible for the largest droplets, as corresponding to a single-mode excitation, for small droplets the radial oscillations are damped and display different oscillatory behaviors (beats), anticipating the presence of several modes in the monopole strength, as the Fourier analysis of the signal unveils.

Figure 5 (right) displays the monopole strength function in logarithmic scale as a function of the excitation frequency. The solid vertical line represents the frequency $|\mu|/\hbar$ corresponding to the atom emission threshold, i.e. the absolute value of the atom chemical potential, $|\mu|$. It can be seen that for $(\tilde{N} - 18.65)^{1/4} = 5.1$ the strength is in the continuum frequency region above $|\mu|/\hbar$. Hence, self-bound small ^{39}K droplets, monopolarly excited, have excited states (resonances) that may decay by atom emission [16, 44]. This decay does not imply that the droplet breaks apart; it just loses the energy deposited into it by emitting a number of atoms, in a way similar to the decay of some states appearing in the atomic nucleus, the so-called "giant resonances" [45]. We want to stress that the multipole strength is not normalized, as it depends on the value of the arbitrary small parameter λ. However, the relative intensity of the peaks for a given droplet is properly accounted for in this approach.

A similar analysis for the quadrupole mode is presented in Fig. 6. In this case, we have found a more harmonic behavior for $\langle Q_2(t)\rangle$, and therefore the quadrupole strength function is dominated by one single peak.

Figures 5 and 6 show an interesting evolution of the strength function from the continuum to the discrete part of the frequency spectrum as the number of atoms in the droplet increases. For small N values, but still corresponding to self-bound quantum droplets, the spectrum is dominated by a broad resonance that may decay by atom emission. The $\langle Q(t)\rangle$ oscillations are damped, and when several resonances are present (monopole case), distinct beats appear in the oscillations.

This remarkable evolution of the monopole and quadrupole spectrum has also been found for ^{3}He and ^{4}He droplets [46, 47]. In the ^{4}He case, it has been experimentally confirmed by detecting "magic" atom numbers in the size distribution of ^{4}He droplets which correspond to especially stable droplets [48]. The magic numbers occur at the threshold sizes for which the excitation modes of the droplet, as calculated by the diffusion Monte Carlo method, are stabilized when they pass below the atom emission energy. This constituted the first experimental confirmation for the energy levels of ^{4}He droplets. On the other hand, in confined BECs, the energy of the breathing mode is obtained by direct analysis of the radial oscillations of the atom cloud [3].

We show in Fig. 7 the breathing and quadrupole frequencies, corresponding to the more intense peaks, as a function of the number of atoms obtained with the QMC functional and the MF+LHY approach. For the latter, our results are in full agreement with those reported by Petrov using the Bovoliubov-de Gennes method [16], which is fully equivalent to ours and to that of Ref. [44], hence the perfect agreement between the three results. The results are plotted in the universal units of the MF+LHY theory. We find that the QMC functional predicts systematically larger monopole and quadrupole frequencies in all the range of particle numbers we have studied. Additionally, as we change the magnetic field, i.e. the scattering parameters, QMC predictions do not fall on the same curve, meaning that the QMC functional breaks the MF+LHY universality.

When the multipole strength is concentrated in a single narrow peak, it is possible to estimate the peak frequency using the sum rules approach [3, 45]. Sum rules are energy moments of the strength function that, for some excitation operators, can be written as compact expressions involving expectation values on the ground state configuration. For the multipole operators considered here, two such sum rules are the linear-energy m_1 and cubic-energy m_3 sum rules. The inverse-energy sum rule m_{-1} can be obtained from a constrained calculation involving the Hamiltonian $\mathcal{H}'$ of Eq. (17). Once determined, these three sum rules may be used to define two average energies $E_1 = \sqrt{m_1/m_{-1}}$ and $E_3 = \sqrt{m_3/m_1}$ expecting, *bona fide*, that they are good estimates of the peak energy.

For the monopole and quadrupole modes, the E_1 energies are [45]

$$E_1(\ell = 0) = \sqrt{-\frac{4\hbar^2}{m}\,\frac{\langle r^2\rangle}{\left(\partial\langle Q_0\rangle/\partial\lambda\right)|_{\lambda=0}}} \tag{20}$$

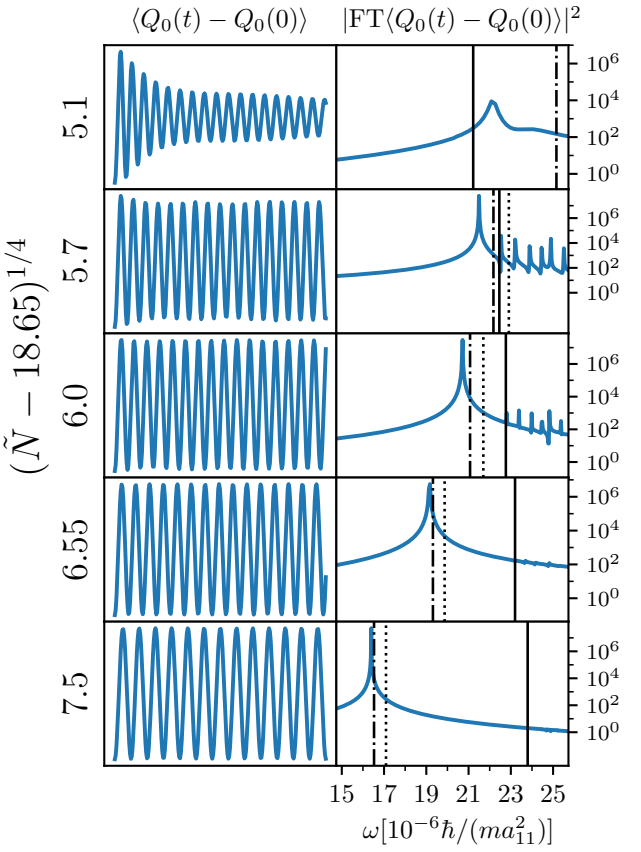

FIG. 5. Time evolution of the monopole moment $\langle Q_0(t)\rangle$ and strength function (right) for ^{39}K quantum droplets of different sizes obtained using the QMC functional at $B = 56.230$ G. In the right panels, the vertical solid line corresponds to the frequency $|\mu|/\hbar$ corresponding to the atom emission energy $|\mu|$, and the dotted and dash-dotted lines to the $E_3/\hbar$ and $E_1/\hbar$ frequencies, obtained by the sum rules in Eq. (23) and (20), respectively.

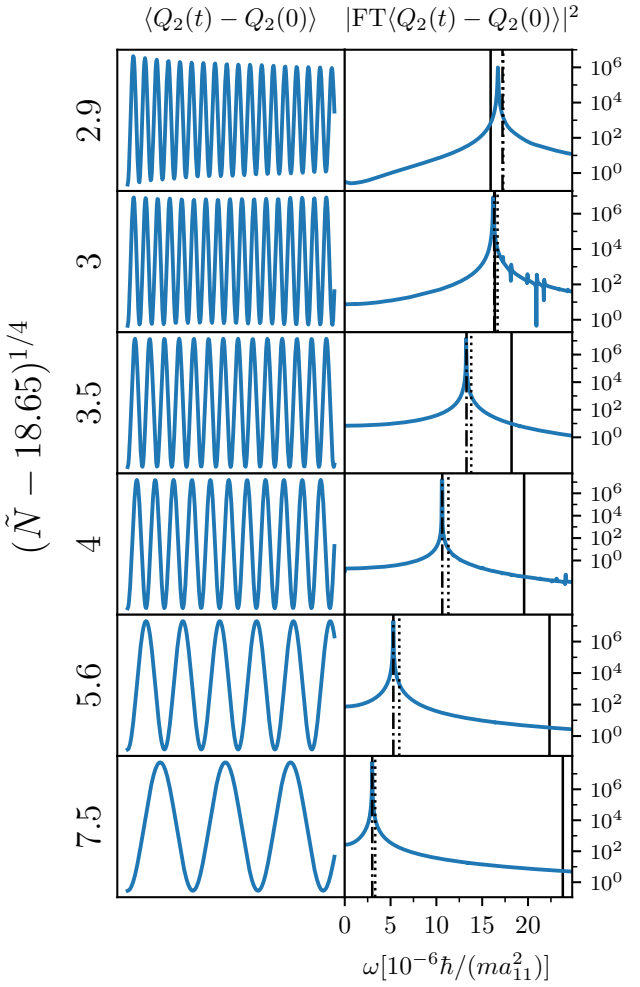

FIG. 6. Time evolution of the quadrupole moment $\langle Q_2(t)\rangle$ and strength function (right) for ^{39}K quantum droplets of different sizes obtained using the QMC functional at $B = 56.230$ G. In the right panels, the vertical solid line corresponds to the frequency $|\mu|/\hbar$ corresponding to the atom emission energy $|\mu|$, and the dotted and dash-dotted lines to the $E_3/\hbar$ and $E_1/\hbar$ frequencies, obtained by the sum rules in Eq. (24) and (21), respectively.

and

$$E_1(\ell = 2) = \sqrt{-\frac{8\hbar^2}{m}\frac{\langle r^2\rangle}{(\partial\langle Q_2\rangle/\partial\lambda)|_{\lambda=0}}}\,, \qquad (21)$$

with λ being the parameter in the constrained Hamiltonian $\mathcal{H}'$, Eq.(17), and $\langle r^2\rangle = \int d\boldsymbol{r}\rho(r)r^2/N$ evaluated at $\lambda = 0$. The frequencies corresponding to these energies are drawn in Figs. 5 and 6 as vertical dash-dotted lines. Except for small droplets, for which the monopole strength is very fragmented, one can see that they are good estimates of the peak frequency.

Closed expressions for the E_3 averages can be easiliy obtained for the monopole and the quadrupole modes [3, 45]. For the sake of completeness, we present the result obtained for the QMC functional.

Defining

$$E_\alpha = \alpha\int d\mathbf{r}\rho^2(\mathbf{r})$$
$$E_\beta = \beta\int d\mathbf{r}\rho^{\gamma+1}(\mathbf{r})$$
$$\langle T\rangle = \frac{\hbar^2}{2m}\int d\mathbf{r}|\nabla\Psi(\mathbf{r})|^2\,, \qquad (22)$$

where $\Psi(\mathbf{r})$ and $\rho(\mathbf{r})$ are those of the equilibrium configuration, we have

$$E_3(\ell = 0) = \left[\frac{\hbar^2}{Nm\langle r^2\rangle}\right]^{1/2}[4\langle T\rangle + 9(E_\alpha + \gamma^2 E_\beta)]^{1/2} \qquad (23)$$

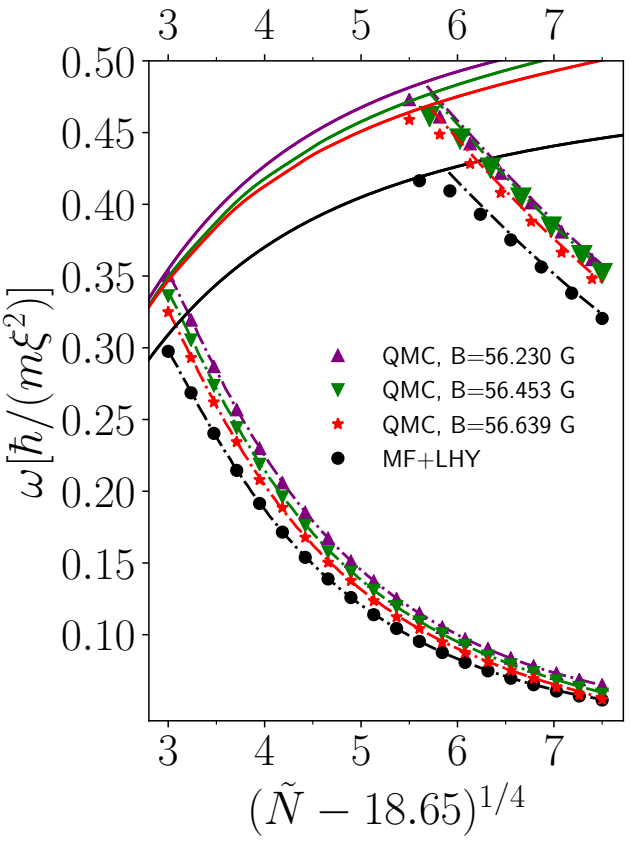

FIG. 7. Breathing (upper points) and quadrupole (lower points) frequencies as a function of the total atom number in units of $\tilde{N}$. Points are the results obtained from QMC and MF+LHY TDDFT calculations, and dashed lines are the $E_1/\hbar$ frequencies from the sum-rule approach (Eqs. (20) and (21)). Full lines represent the frequency corresponding to the absolute value of the droplet chemical potential $|\mu|$, corresponding to the legend from top to bottom

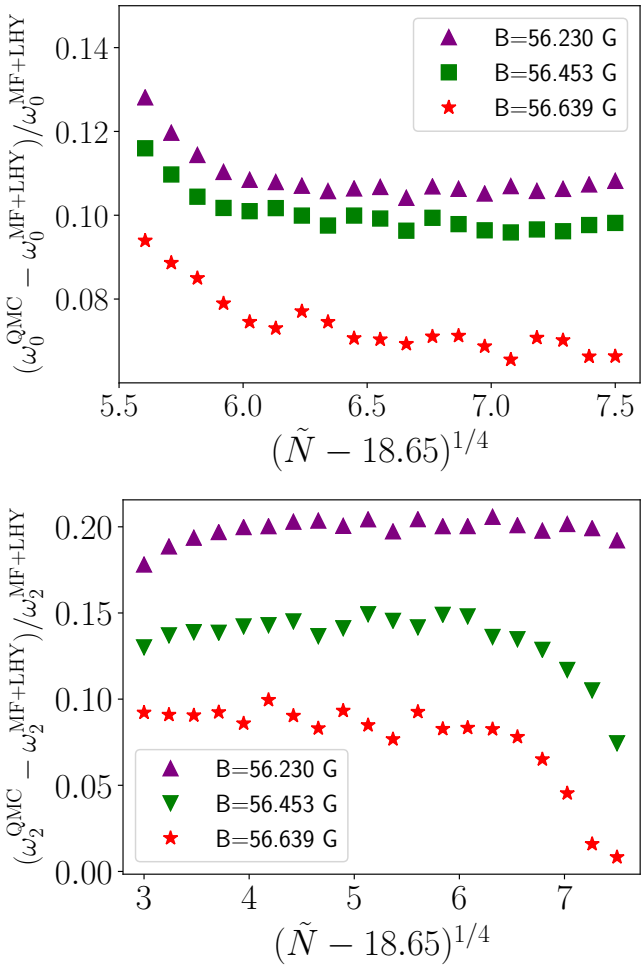

FIG. 8. Relative frequency difference between QMC and MF+LHY TDDFT calculations for quadrupole (bottom figure) and monopole modes (top figure) as a function of the total atom number in units of $\tilde{N}$.

$$E_3(\ell=2)=\left[\frac{\hbar^2}{Nm\langle r^2\rangle}\right]^{1/2}[4\langle T\rangle]^{1/2}\,. \qquad (24)$$

We have $E_3(\ell=2)<E_3(\ell=0)$. The $\omega_3=E_3/\hbar$ frequencies are shown in Figs. 5 and 6 as vertical dotted lines. It can be seen that even when the strength is concentrated in a single peak, ω_3 is a worse estimate of the peak frequency than $\omega_1=E_1/\hbar$. This is likely so because m_3 gets contributions from the high energy part of the spectrum. At variance, since contributions to m_{-1} mainly come from the low energy part of the spectrum, ω_1 is better suited for estimating the peak frequency.

The relative differences between the MF+LHY theory and the QMC functional for monopole and quadrupole frequencies are presented in Fig. 8. As the magnetic field increases, the droplet is more correlated and differences of even 20% can be observed.

We finally compare in more detail the frequencies obtained with the QMC and MF+LHY functionals at $B=56.230$ G for $\tilde{N}=100$ and $\tilde{N}=1010$, which correspond to $N=7\times10^4$ and $N=7.1\times10^5$, respectively. Although it might require rather large droplets to observe neat breathing oscillations, systems with $\tilde{N}>100$, for which clean quadrupole modes show up (see Fig. 7), are already accessible in experiments [19, 20, 22, 33]. For $N=7\times10^4$, the quadrupole frequencies are $\omega_2^{\rm QMC}=2323\,$Hz and $\omega_2^{\rm MF+LHY}=1972\,$Hz, i.e. oscillation periods $\tau_2^{\rm QMC}=2.70\,$ms and $\tau_2^{\rm MF+LHY}=3.19\,$ms. A similar comparison can be made for the monopole frequency; for $N=7.1\times10^5$, the frequencies are $\omega_0^{\rm QMC}=3114\,$Hz and $\omega_0^{\rm MF+LHY}=2755\,$Hz, and the oscillation periods are $\tau_0^{\rm QMC}=2.02\,$ms, and $\tau_0^{\rm MF+LHY}=2.28\,$ms. In Fig. (9), we report our results for the breathing and quadrupole modes in not-reduced units to facilitate future comparisons with experiments.

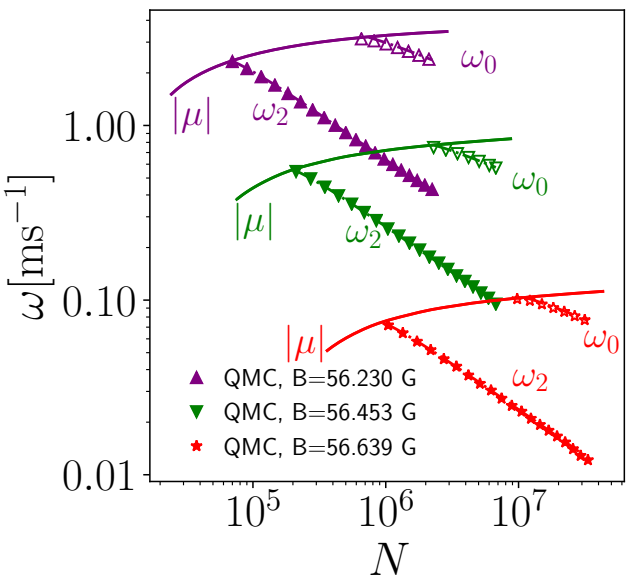

FIG. 9. Predictions of the frequency corresponding to the absolute value of the chemical potential $|\mu|$, breathing frequency ω_0 and quadropole frequency ω_2 as a function of total atom number, using the QMC functionals. Dashed lines are $\omega_1 = E_1/\hbar$ frequencies.

V. SUMMARY AND OUTLOOK

Using a new QMC-based density functional which properly incorporates finite-range effects, we have determined the monopole and quadrupole excitation modes of ^{39}K quantum droplets at the optimal MF+LHY mixture composition. Comparing with the results obtained within the MF+LHY approach, we have found that finite-range effects have a detectable influence on the excitation spectrum, whose study may thus be a promising way to explore physics beyond the LHY correction.

We have shown that introducing the QMC functional into the usual DFT methodology can easily be done, as only minor changes need to be made in the (many) existing Gross-Pitaevskii numerical solvers [49–51]. This opens the door to using better functionals –based on including quantum effects beyond mean-field– in the current applications of the extended Gross-Pitaevskii approach [33, 52].

The significant difference between the predictions of QMC and MF+LHY functionals for the excitation spectrum indicates that finite-range effects could show up in other dynamical problems as well. In particular, in droplet-droplet collisions [33], where the actual value of the incompressibility might play a relevant role. A reliable functional might also be useful to study quantum droplet aspects that are currently under study for superfluid ^{4}He droplets, as the appearance of quantum turbulence and of bulk and surface vorticity in droplets merging; the equilibrium phase diagram of rotating quantum droplets [53–55], and the merging of vortex-hosting quantum droplets. These aspects are at present under investigation. Further improvements in the building of a more accurate QMC functional should consider the inclusion of surface tension effects others that those arising from the quantum kinetic energy term [56].

ACKNOWLEDGMENTS

This work has been supported by the Ministerio de Economia, Industria y Competitividad (MINECO, Spain) under grants Nos. FIS2017-84114-C2-1-P and FIS2017-87801-P (AEI/FEDER, UE), and by the EC Research Innovation Action under the H2020 Programme, Project HPC-EUROPA3 (INFRAIA-2016-1-730897). V. C. gratefully acknowledges the support of G. E. Astrakharchik at the UPC and the computer resources and technical support provided by Barcelona Supercomputing Center. We acknowledge financial support from Secretaria d'Universitats i Recerca del Departament d'Empresa i Coneixement de la Generalitat de Catalunya, co-funded by the European Union Regional Development Fund within the ERDF Operational Program of Catalunya (project QuantumCat, ref. 001-P-001644).

[1] I. Bloch, J. Dalibard, and W. Zwerger, Rev. Mod. Phys. **80**, 885 (2008).
[2] C. J. Pethick and H. Smith, Bose-Einstein condensation in dilute gases (Cambridge University Press, 2008).
[3] L. Pitaevskii and S. Stringari, Bose-Einstein condensation and superfluidity, Vol. 164 (Oxford University Press, 2016).
[4] N. Bogoliubov, J. Phys. (USSR) **11**, 23 (1947).
[5] V. Cikojević, K. Dželalija, P. Stipanović, L. Vranješ Markić, and J. Boronat, Phys. Rev. B **97**, 140502(R) (2018).
[6] V. Cikojević, L. V. Markić, G. E. Astrakharchik, and J. Boronat, Phys. Rev. A **99**, 023618 (2019).
[7] L. Parisi and S. Giorgini, arXiv preprint arXiv:2003.05231 (2020).
[8] L. Parisi, G. E. Astrakharchik, and S. Giorgini, Phys. Rev. Lett **122**, 105302 (2019).
[9] C. Staudinger, F. Mazzanti, and R. E. Zillich, Phys. Rev. A **98**, 023633 (2018).
[10] D. S. Petrov and G. E. Astrakharchik, Phys. Rev. Lett **117**, 100401 (2016).
[11] R. Bombin, J. Boronat, and F. Mazzanti, Phys. Rev. Lett **119**, 250402 (2017).
[12] F. Ancilotto, M. Barranco, M. Guilleumas, and M. Pi, Phys. Rev. A **98**, 053623 (2018).

[13] H. Hu and X.-J. Liu, arXiv preprint arXiv:2005.08581 (2020).
[14] H. Hu and X.-J. Liu, arXiv preprint arXiv:2006.00434 (2020).
[15] M. Ota and G. E. Astrakharchik, arXiv preprint arXiv:2005.10047 (2020).
[16] D. S. Petrov, Phys. Rev. Lett **115**, 155302 (2015).
[17] T. D. Lee, K. Huang, and C. N. Yang, Phys. Rev. **106**, 1135 (1957).
[18] M. Barranco, R. Guardiola, S. Hernández, R. Mayol, J. Navarro, and M. Pi, J. Low Temp. Phys. **142**, 1 (2006).
[19] C. Cabrera, L. Tanzi, J. Sanz, B. Naylor, P. Thomas, P. Cheiney, and L. Tarruell, Science **359**, 301 (2018).
[20] G. Semeghini, G. Ferioli, L. Masi, C. Mazzinghi, L. Wolswijk, F. Minardi, M. Modugno, G. Modugno, M. Inguscio, and M. Fattori, Phys. Rev. Lett **120**, 235301 (2018).
[21] P. Cheiney, C. R. Cabrera, J. Sanz, B. Naylor, L. Tanzi, and L. Tarruell, Phys. Rev. Lett **120**, 135301 (2018).
[22] C. D'Errico, A. Burchianti, M. Prevedelli, L. Salasnich, F. Ancilotto, M. Modugno, F. Minardi, and C. Fort, Phys. Rev. Research **1**, 033155 (2019).
[23] V. Cikojević, L. V. Markić, and J. Boronat, New J. Phys **22**, 053045 (2020).
[24] L. Tanzi, C. R. Cabrera, J. Sanz, P. Cheiney, M. Tomza, and L. Tarruell, Phys. Rev. A **98**, 062712 (2018).
[25] R. G. Newton, Scattering Theory of Waves and Particles (Springer Science & Business Media, 2013).
[26] A. Tononi, Condens. Matter **4**, 20 (2019).
[27] A. Tononi, A. Cappellaro, and L. Salasnich, New J. Phys **20**, 125007 (2018).
[28] L. Salasnich, Phys. Rev. Lett **118**, 130402 (2017).
[29] J. Boronat and J. Casulleras, Phys. Rev. B **49**, 8920 (1994).
[30] S. Giorgini, J. Boronat, and J. Casulleras, Phys. Rev. A **60**, 5129 (1999).
[31] N. B. Jørgensen, G. M. Bruun, and J. J. Arlt, Phys. Rev. Lett **121**, 173403 (2018).
[32] S. Roy, M. Landini, A. Trenkwalder, G. Semeghini, G. Spagnolli, A. Simoni, M. Fattori, M. Inguscio, and G. Modugno, Phys. Rev. Lett **111**, 053202 (2013).
[33] G. Ferioli, G. Semeghini, L. Masi, G. Giusti, G. Modugno, M. Inguscio, A. Gallemí, A. Recati, and M. Fattori, Phys. Rev. Lett **122**, 090401 (2019).
[34] S. Stringari and J. Treiner, Phys. Rev. B **36**, 8369 (1987).
[35] F. Ancilotto, M. Barranco, F. Coppens, J. Eloranta, N. Halberstadt, A. Hernando, D. Mateo, and M. Pi, Int. Rev. Phys. Chem. **36**, 621 (2017), https://doi.org/10.1080/0144235X.2017.1351672.
[36] S. A. Chin, S. Janecek, and E. Krotscheck, Chemical Phys. Let. **470**, 342 (2009).
[37] S. A. Chin, Phys. Rev. E **76**, 056708 (2007).
[38] F. Dalfovo, S. Giorgini, L. P. Pitaevskii, and S. Stringari, Rev. Mod. Phys. **71**, 463 (1999).
[39] D. Baillie, R. M. Wilson, and P. B. Blakie, Phys. Rev. Lett **119**, 255302 (2017).
[40] S. Stringari and D. Vautherin, Phys. Let. B **88**, 1 (1979).
[41] M. Pi, M. Barranco, J. Nemeth, C. Ngô, and E. Tomasi, Phys. Let. B **166**, 1 (1986).
[42] D. S. Jin, J. R. Ensher, M. R. Matthews, C. E. Wieman, and E. A. Cornell, Phys. Rev. Lett **77**, 420 (1996).
[43] A. Altmeyer, S. Riedl, C. Kohstall, M. J. Wright, R. Geursen, M. Bartenstein, C. Chin, J. H. Denschlag, and R. Grimm, Phys. Rev. Lett **98**, 040401 (2007).
[44] G. Ferioli, G. Semeghini, S. Terradas-Briansó, L. Masi, M. Fattori, and M. Modugno, Phys. Rev. Research **2**, 013269 (2020).
[45] O. Bohigas, A. Lane, and J. Martorell, Phys. Rep. **51**, 267 (1979).
[46] L. Serra, J. Navarro, M. Barranco, and N. Van Giai, Phys. Rev. Lett **67**, 2311 (1991).
[47] M. Barranco and E. S. Hernández, Phys. Rev. B **49**, 12078 (1994).
[48] R. Brühl, R. Guardiola, A. Kalinin, O. Kornilov, J. Navarro, T. Savas, and J. P. Toennies, Phys. Rev. Lett **92**, 185301 (2004).
[49] X. Antoine and R. Duboscq, Comput. Phys. Commun **193**, 95 (2015).
[50] P. Wittek and L. Calderaro, Comput. Phys. Commun **197**, 339 (2015).
[51] J. R. Schloss and L. J. O'Riordan, J. Open Source Softw **3**, 1037 (2018).
[52] G. E. Astrakharchik and B. A. Malomed, Phys. Rev. A **98**, 013631 (2018).
[53] F. Ancilotto, M. Barranco, and M. Pi, Phys. Rev. B **97**, 184515 (2018).
[54] J. M. Escartín, F. Ancilotto, M. Barranco, and M. Pi, Phys. Rev. B **99**, 140505(R) (2019).
[55] S. M. O. O'Connell, R. M. P. Tanyag, D. Verma, C. Bernando, W. Pang, C. Bacellar, C. A. Saladrigas, J. Mahl, B. W. Toulson, Y. Kumagai, P. Walter, F. Ancilotto, M. Barranco, M. Pi, C. Bostedt, O. Gessner, and A. F. Vilesov, Phys. Rev. Lett. **124**, 215301 (2020).
[56] J. M. Marín, J. Boronat, and J. Casulleras, Phys. Rev. B **71**, 144518 (2005).